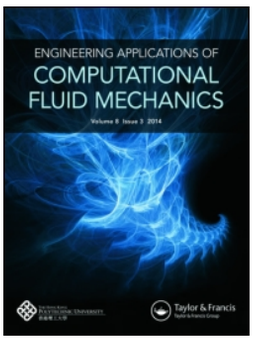

Taylor & Francis
Taylor & Francis Group

Engineering Applications of Computational Fluid Mechanics

ISSN: 1994-2060 (Print) 1997-003X (Online) Journal homepage: https://www.tandfonline.com/loi/tcfm20

Effects of aspect ratio, wall thickness and hypertension in the patient-specific computational modeling of cerebral aneurysms using fluid-structure interaction analysis

Hong Tao Sun, Kam Yim Sze, Abraham Yik Sau Tang, Anderson Chun On Tsang, Alfred Cheuk Hang Yu & Kwok Wing Chow

To cite this article: Hong Tao Sun, Kam Yim Sze, Abraham Yik Sau Tang, Anderson Chun On Tsang, Alfred Cheuk Hang Yu & Kwok Wing Chow (2019) Effects of aspect ratio, wall thickness and hypertension in the patient-specific computational modeling of cerebral aneurysms using fluid-structure interaction analysis, Engineering Applications of Computational Fluid Mechanics, 13:1, 229-244, DOI: 10.1080/19942060.2019.1572540

To link to this article: https://doi.org/10.1080/19942060.2019.1572540

Published online: 10 Feb 2019.

ENGINEERING APPLICATIONS OF COMPUTATIONAL FLUID MECHANICS
2019, VOL. 13, NO. 1, 229–244
https://doi.org/10.1080/19942060.2019.1572540

Effects of aspect ratio, wall thickness and hypertension in the patient-specific computational modeling of cerebral aneurysms using fluid-structure interaction analysis

Hong Tao Sun[a], Kam Yim Sze[a], Abraham Yik Sau Tang[a], Anderson Chun On Tsang[b], Alfred Cheuk Hang Yu[c] and Kwok Wing Chow[a]

[a]Department of Mechanical Engineering, The University of Hong Kong, Pokfulam, Hong Kong; [b]Department of Surgery, Li Ka Shing Faculty of Medicine,The University of Hong Kong, Pokfulam, Hong Kong; [c]Department of Electrical and Computer Engineering, University of Waterloo, Waterloo, ON, Canada

ABSTRACT

Intracranial aneurysm is a pathological dilatation of the cerebral artery which can lead to high mortality rate upon rupture. The aspect ratio (AR) of an aneurysm, being the ratio of the height to neck width, is an important factor in estimating the likelihood of aneurysm rupture in clinical practice. AR will generally increase while the aneurysm grows. Clinical observations over the years show that aneurysms with larger AR usually exhibit higher rupture risk. The goal of the current study is to conduct Fluid-Structure Interaction (FSI) analyses to provide quantitative estimates on the importance of AR, wall thickness (t_w) and hypertension. The effects of varying AR and t_w on the hemodynamics, wall stress and displacement will be studied based on patient-specific models. Both sidewall and bifurcation aneurysms are investigated. There is a significant increase in the wall stress at the aneurysmal dome (the location in an aneurysm where rupture is commonly observed clinically) when the AR increases and t_w decreases due to the aneurysm growth process. Furthermore, these investigations are repeated for patients with hypertension (high blood pressure) conditions. The increase in the wall stress due to hypertension for models with higher ARs is more dramatic. The clinically observed feature of higher rupture risk of aneurysms with larger AR is thus supported quantitatively.

ARTICLE HISTORY
Received 2 January 2018
Accepted 16 January 2019

KEYWORDS
Intracranial aneurysms; fluid-structure interaction; FSI; aspect ratio; wall thickness; hypertension

1. Introduction

Abnormal dilation of the artery, termed aneurysm, can be life-threatening. Rupture of an intracranial aneurysm (IA) can lead to massive internal bleeding in the subarachnoid space. The occurrence rate of IA is 2% to 5% in the population (Humphrey & Taylor, 2008) and aneurysm rupture also leads to high mortality rate (Sforza, Putman, & Cebral, 2009). A typical geometric parameter of the aneurysm is the aspect ratio (AR) which is defined as the ratio of the aneurysm height to the equivalent diameter ($=\text{circumference}/\pi$) of the aneurysm neck. Clinical analysis reported that aneurysms with AR greater than 1.6 are prone to rupture (Ujiie, Tamano, Sasaki, & Hori, 2001). Several types of endovascular surgical treatment including coiling and flow diverter stenting are available for mitigating the risk of rupture.

The underlying mechanism of aneurysm rupture is complicated and not well understood. Intensive computational studies have been performed to assess the rupture risk of an IA and the post-treatment response (Ahmed, Šutalo, Kavnoudias, & Madan, 2011; Berg et al., 2015; Ford, Lee, Lownie, Holdsworth, & Steinman, 2008a; Nair et al., 2016; Tang et al., 2015; Varble, Xiang, Lin, Levy, & Meng, 2016; Zhang, Chong, & Qian, 2013). The influence of the geometry of the aneurysm (in particular AR) and the nearby vasculature on the risk of rupture has been investigated computationally and experimentally (Hoi, Wasserman, Lakatta, & Steinman, 2010; Lai et al., 2016). The hemodynamics inside the aneurysm would play an important role. Computational results have been compared with in vivo magnetic resonance imaging (MRI) measurement and particle imaging velocimetry (PIV) in experiments (Ford et al., 2008b; Rayz et al., 2008). However, many investigations have been conducted based on the rigid wall assumption (Inthavong, Wen, Tu, & Tian, 2009; McGarry, Hitt, & Harris, 2008; Tang, Fan, Cheng, & Chow, 2012). Since the arterial and the aneurysm walls are elastic, taking the wall motion and dilatation into account may provide additional insight on analysing aneurysm rupture risk.

CONTACT Hong Tao Sun htsun@hku.hk

Fluid-structure interaction (FSI) analyses simulate the interaction between fluid and solid domains by incorporating fluid dynamics, structural/solid mechanics as well as the coupling between the fluid and solid domains. Biomechanical factors including arterial and aneurysm geometries, thickness of the aneurysm wall (t_w), blood pressure, outflow/inflow conditions and a measure of fluid friction, namely, the wall shear stress (*WSS*) have been investigated (Torii, Oshima, Kobayashi, Takagi, & Tezduyar, 2011). The arterial and the aneurysm geometries are believed to play a critical role in the process of rupture. A curved parent vessel might be associated with greater risk of aneurysmal wall damage (Ahmed et al., 2011). The effect of AR scaled to the range of 0.3–2.0 had been investigated with FSI using patient models (Long et al., 2015). As AR increases, energy loss per unit aneurysmal volume increases and is used to assess rupture risk (Long et al., 2015). However, the stress of the aneurysmal wall and the spatial variation of such stress have not been reported.

Besides AR, t_w is another critical parameter (Sanchez et al., 2013; Torii, Oshima, Kobayashi, Takagi, & Tezduyar, 2010; Valencia & Solis, 2006). It can influence the dilatational variation of an aneurysm in the cardiac cycle (Sanchez et al., 2013). Moreover, utilizing a pathologically realistic t_w of 0.05 mm can affect the wall displacement and *WSS* by more than 50% compared to a model with a normal, uniform t_w of 0.3 mm (Torii et al., 2010). Indeed, it can be well-expected that a smaller t_w would lead to larger wall displacement and stress (Valencia & Solis, 2006). FSI analyses utilizing patient-specific t_w have also been performed (Voß et al., 2016). Besides effects due to geometry, dynamical factors like hypertension and pressure gradient also affect the rupture risk (Ahmed et al., 2011; Long et al., 2015; Valencia & Torres, 2017) through changes in the wall stress of the aneurysm and *WSS* (Ahmed et al., 2011; Lee, Zhang, Takao, Murayama, & Qian, 2013). A comparison between pre-ruptured and unruptured aneurysms has also been undertaken (Lee et al., 2013). The former entities were constructed with imaging data just before rupture. Larger displacement at the dome region, lower *WSS* and a higher wall stress are observed in the pre-rupture state. However, the effects of AR increase and t_w reduction due to aneurysm growth have not been incorporated in all these previous studies (Ahmed et al., 2011; Lee et al., 2013; Sanchez et al., 2013; Torii et al., 2011; Valencia et al., 2013; Valencia & Torres, 2017).

In the current study four patient-specific aneurysm models, consisting of two sidewall and two bifurcation cases, were used to study how the AR increase and t_w reduction arising from aneurysm scaling would affect the blood hemodynamics and the wall stress. The *WSS*, wall stress and wall displacement are commonly used to assess the rupture risk as the aneurysm grows. Our results show that all these quantities evolve with the AR increase and t_w reduction in the way that the IA rupture risk becomes higher. It is also noted that an aneurysm with a higher AR after scaling would also exhibit a long-term low *WSS* scenario under the condition of hypertension, further enhancing the rupture risk.

2. Methods

2.1. Geometric configuration

Four patients with IA were selected for the FSI analysis. The consent of the patients and the approval by the Institutional Review Board of the Hospital were obtained. The morphology of the aneurysm and the nearby vasculature were obtained by standard imaging procedures (Figure 1). For Patient A, computed tomography angiograms (CTAs) were produced by the Toshiba Medical Systems Corporation (in-plane resolution 0.43 mm, slice thickness 0.50 mm) with the aid of a contrast agent. For Patient B, magnetic resonance angiograms (MRAs) were produced by the Signa Excite scanner manufactured by GE Medical Systems (in-plane resolution 0.47 mm, slice thickness 1.00 mm). For Patients C and D, CTAs were produced by the LightSpeed VCT scanner manufactured by the GE Medical Systems (in-plane resolution 0.27 mm, slice thickness 0.63 mm) with the aid of contrast agent. Based on these imaging data, three-dimensional models were constructed by selecting the solid-fluid boundary for every slice in the software Mimics 18.0 (Materialise, Leuven, Belgium) (Tang et al., 2015). These geometric configurations were then exported in STL format, and were smoothed by

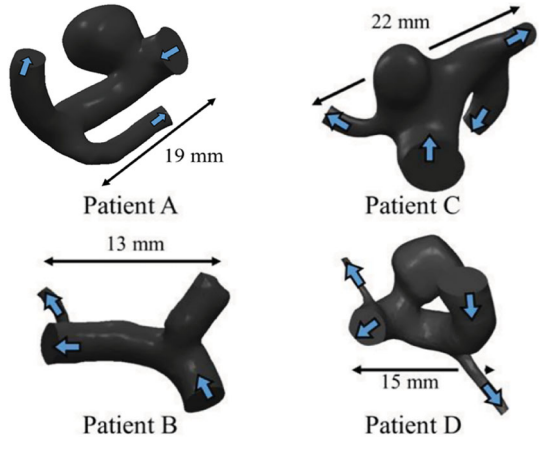

Figure 1. Geometric configurations of patient-specific models. Blue arrows indicate the flow direction inside the models.

Table 1. Information on the patients and geometric configurations.

Model	Gender	Age	Aneurysm type	Aspect ratio	Aneurysmal volume (mm^3)
Patient A	F	71	Sidewall Aneurysm	1.5	938.8
Patient B	F	36	Sidewall Aneurysm	1.9	207.8
Patient C	F	61	Bifurcation Aneurysm	1.2	538.3
Patient D	F	75	Bifurcation Aneurysm	2.2	633.4

SOLIDWORKS 2016 and its reverse engineering add-in ScanTo3D. Since the precision of the imaging data was not sufficient to resolve the aneurysm wall, the wall thickness of the models was assumed to be uniform. Selected information on the patients and the geometric configurations of the aneurysms were provided in Table 1.

2.2. The scaling method

When the aneurysm grows, AR increases and t_w reduces. To study the effect of AR and t_w on the blood hemodynamics and the wall stress, the patient-specific aneurysm models were scaled to create the models with higher ARs and lower t_ws by noting that expansion of the aneurysm increases monotonically from the neck to the dome during the aneurysm grows (Kroon, 2011) and the t_w of ruptured aneurysms can be as thin as 0.05 mm (Abruzzo el al., 1998). The following scaling procedure was formulated:

(1) The necking plane, being the narrowest transverse section of the aneurysm, was visually identified. Normal to the neck defines the longitudinal coordinate V as shown in Figure 2. V is taken as zero at the necking plane.
(2) $V_{\max}$, the value of V at the highest point of the dome, was measured.
(3) At any V termed V_c, the boundary contour of the aneurysm was extracted. The contour was shifted to $V = \alpha V_c$ where α was a scaling factor to be defined in the next step. The contour was also expanded transversely and normal to the contour by a constant offset equal to $(\alpha - 1)$ times the effective diameter of the contour before expansion.
(4) There was no expansion below the necking plane, i.e. $\alpha = 1$ for $V < 0$. The factor α increased linearly

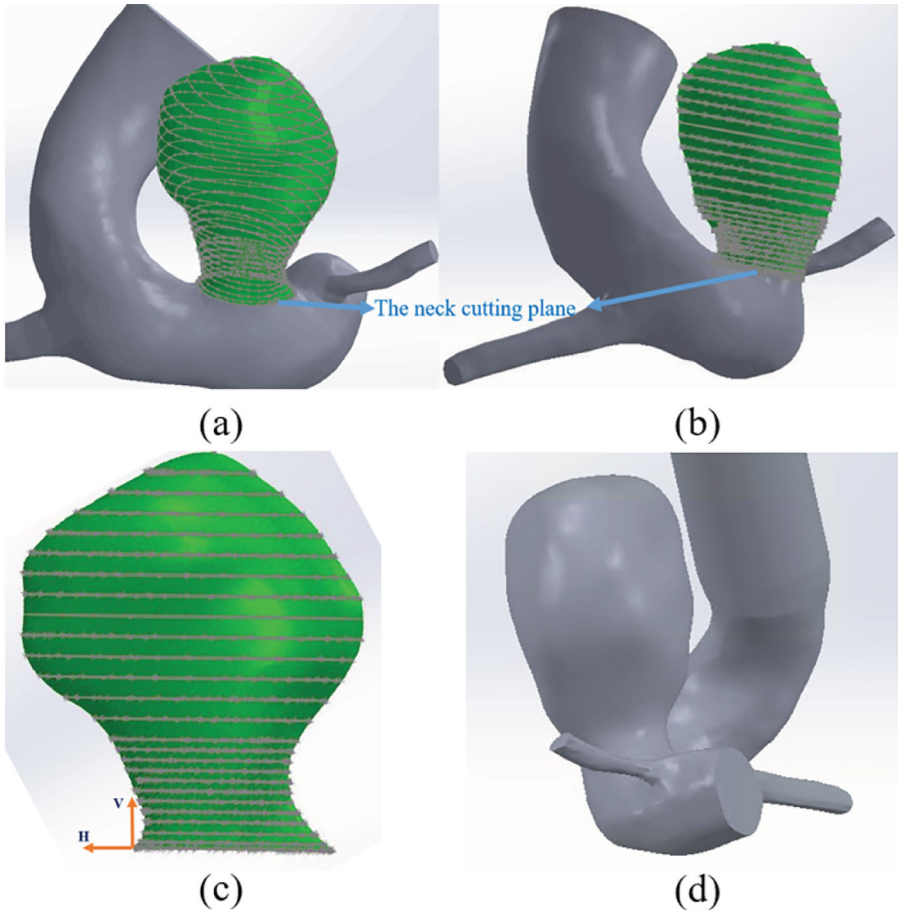

Figure 2. The illustration of the proposed scaling method, based on the geometry of Patient D.

from unity at $V = 0$ to $\alpha_{\max}$ at $V = V_{\max}/3$ and remained at $\alpha_{\max}$ for $V > V_{\max}/3$. $\alpha_{\max}$ was determined by keeping the tissue volume, equal to the integral of t_w over the surface area of the aneurysm, constant and t_w after the scaling to be 50% of that before the expansion.

A constant α instead of the linearly increasing α was used for $V > V_{\max}/3$, as the morphology of the aneurysm would be seriously distorted otherwise. For instance, a cylindrical aneurysm will become the one with a much larger dome. By trial and error, $\alpha_{\max}$ was determined to be 1.28, 1.26, 1.27 and 1.24 whilst the ARs after growth were 1.8, 2.3, 1.5 and 2.6 for the models of Patients A, B, C and D, respectively.

2.3. Governing equations

2.3.1. Fluid model

Computational simulations of fluid motion are often conducted through Eulerian meshes fixed in space. On the other hand, deformations of the solid materials are often considered by Lagrangian meshes which deform with the material. While the treatment of moving boundary/interface is trivial in Lagrangian meshes, the fluid displacement would quickly ruin the mesh quality. The Arbitrary-Lagrangian-Eulerian formulation (ALE) is a hybrid technique that captures the merits and minimizes the deficiencies of the Eulerian and Lagrangian descriptions. ALE formulation is commonly used for FSI simulations (Badia, Nobile, & Vergara, 2009). The term 'arbitrary' refers to the arbitrary mesh motion to be determined by the user or the software (Belytscho, Liu, Moran, & Elkhodary, 2014). In FSI, the boundary of the fluid mesh often follows the fluid-structure interface. Mass conservation (continuity) and momentum balance (Navier-Stokes equation) can be expressed as:

$$\nabla \cdot \mathbf{u}_f = 0, \tag{1}$$

$$\rho_f \left[\frac{\partial \mathbf{u}_f}{\partial t} + ((\mathbf{u}_f - \mathbf{u}_g) \cdot \nabla)\mathbf{u}_f \right] = \nabla \cdot \boldsymbol{\sigma}_f, \tag{2}$$

in which $\nabla = \{\partial/\partial x, \partial/\partial y, \partial/\partial z\}^T$ is the gradient operator, $\boldsymbol{u}_f$ is the fluid velocity, $\boldsymbol{u}_g$ is the moving coordinate velocity, ρ_f is the fluid density, $\boldsymbol{\sigma}_f = \boldsymbol{\tau} - \mathbf{I}_3 p$ is the fluid stress, p is the pressure and $\boldsymbol{\tau}$ is the shear stress. Furthermore,

$$\boldsymbol{\tau} = \mu[\nabla \mathbf{u}_f^T + (\nabla \mathbf{u}_f^T)^T], \tag{3}$$

where μ is viscosity.

Although blood may exhibit non-Newtonian fluid characteristics and its viscosity can decrease with increasing the shear rate, recent works have shown that the non-Newtonian effect is significant only in very small vessels with diameter less than 0.1 mm (Ku, Elkins, & Taylor, 2005; Perktold, Kenner, Hilbert, Spork, & Florian, 1988). Hence, Newtonian flow was assumed whilst the typical properties $\rho_f = 1\,050\,\text{kg/m}^3$ and $\mu = 0.004\,\text{Pa·s}$ were adopted here (Tang et al., 2015). As the maximum Reynolds number in the current models is 619, due to the systolic velocity 0.342 m/s and the 6.9 mm inlet diameter of Patient C, the flow could be treated as laminar.

2.3.2. Solid model

The deformation of the vessel and aneurysmal walls can readily be described by the Lagrangian description. The momentum balance equation can be expressed as:

$$\nabla \cdot \boldsymbol{\sigma}_s = \rho_s \ddot{\mathbf{u}}_g, \tag{4}$$

where $\boldsymbol{\sigma}_s$ is the Cauchy or, equivalently, the true stress tensor, ρ_s is solid density and $\ddot{\mathbf{u}}_g$ is the local acceleration of the solid.

Because the wall of the intracranial arteries was not thick enough to be resolved in CT and MRI images, a uniform t_w (10% of the diameter (Riley, Barnes, Evans, & Burke, 1992)) was assumed here for the models before growth process. The arterial and aneurysmal walls were assumed to be a Mooney-Rivlin hyperelastic material with the following strain energy function

$$W = c_1(I_1 - 3) + c_2(I_2 - 3) + c_3(I_1 - 3)(I_2 - 3) + c_4(I_1 - 3)^2 + c_5(I_2 - 3)^2, \tag{5}$$

where $c_1 = 0.429$, $c_2 = -0.119$, $c_3 = 0.585$, $c_4 = 0.579$ and $c_5 = 0.564\,\text{MPa}$ (Valencia et al., 2015); I_1 and I_2 are the first and second strain invariants of the Cauchy-Green deformation tensor. For this nonlinear material, the elastic modulus under small strain is equal to $6(c_1 + c_2)$, i.e. 1.86 MPa.

2.4. Boundary conditions

2.4.1. Fluid domain

To mimic the physiological deformation of the arterial wall, a pulsatile and cyclic volume flow rate resembling the real flow conditions in patients is specified at the inlet (Ku, Giddens, Zarins, & Glagov, 1985) (Figure 3). To achieve a fully-developed flow before the aneurysm, the computation domain was extended at the inlet section by a length proportional to the specific Reynolds number using the Extrude function of SOLIDWORKS (Figure 4). Pulsatile pressure with maximum/minimum values 120/80 and 160/100 mmHg were employed at the outlet(s) (Lee et al., 2013). The former set of pressures was the normal range whilst the latter was adopted to investigate the effect of hypertension (Figure 3).

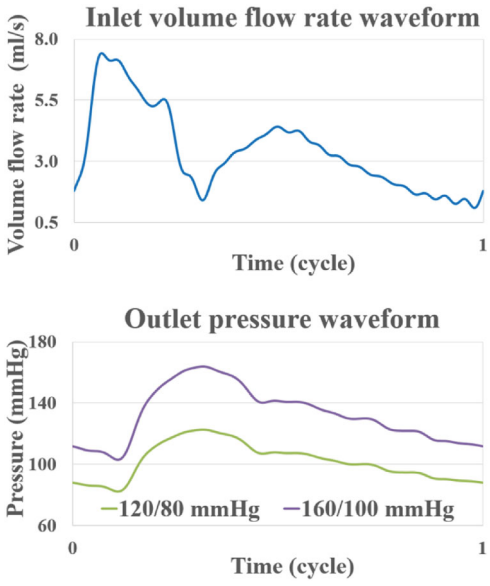

Figure 3. Pulsatile volume flow rate at the inlet and pulsatile pressures at the outlets. Pressure waveforms with 160/100 mmHg refer to hypertension cases described in Section 3.4.

2.4.2. Solid domain

The solid domain composed of the vessel and aneurysm walls is modeled by 3D-shell elements of ADINA. The elements consider all components of stress and strain, i.e. thin shell assumptions such as zero transverse normal and shear are not adopted. The nodal parameters of the 3D-shell elements include 3 translations, 2 or 3 rotations, thickness strain and linear varying thickness strain. Mixed Interpolation of Tensorial Components (MITC) and the displacement/pressure (u/p) formulation are employed to circumvent shear and volumetric lockings, respectively (Sussman & Bathe, 2013). The latter arises when the materials are incompressible or nearly incompressible. Indeed, the adopted hyperelastic material model is incompressible. Gravity is ignored and the nodes of the shell finite elements at the inlet and outlet sections are restrained from motion. These are the common practices of FSI simulations (Bazilevs et al., 2010; Lee et al., 2013; Valencia, Ledermann, Rivera, Bravo, & Galvez, 2008).

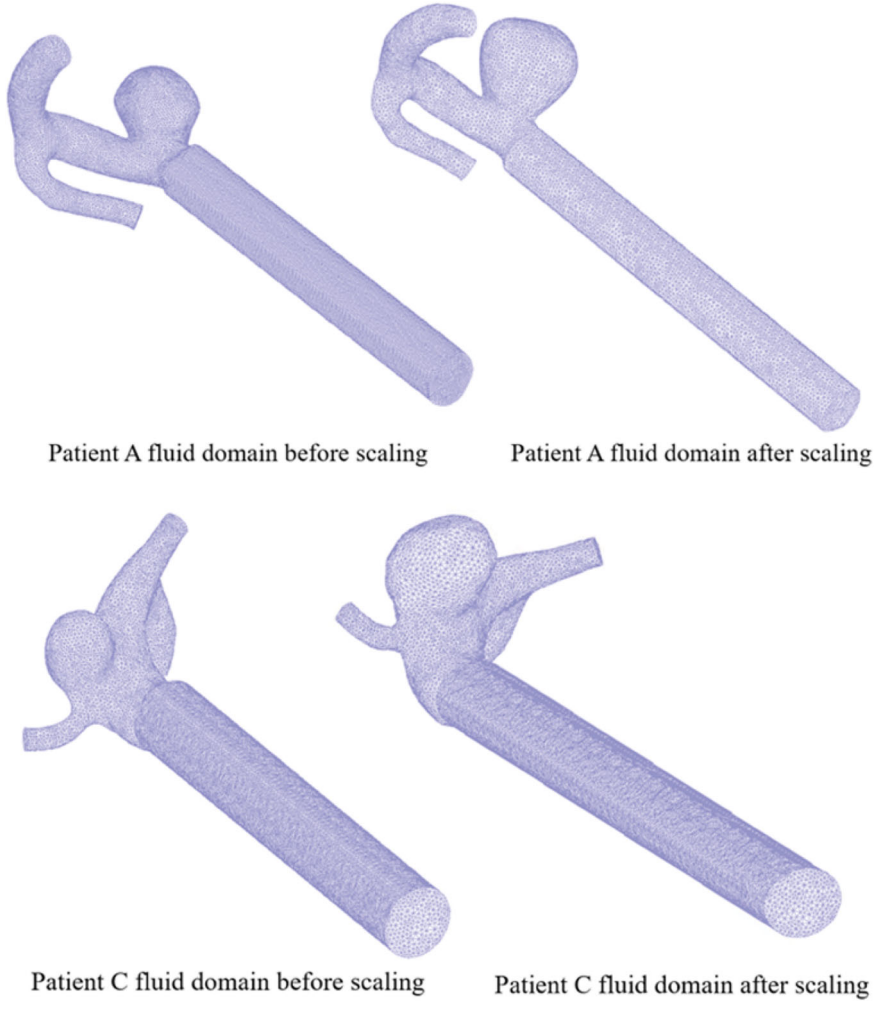

Figure 4. The meshes of fluid domains for Patient A and Patient C.

2.4.3. Conditions at the fluid-structural interface

For the computational simultions, the no-slip condition was assumed (Valencia et al., 2008). Thus, the fluid displacemnet $\mathbf{d}_f$ and the solid displacement $\mathbf{d}_s$ at the fluid-structure interface should be compatible, i.e.

$$\mathbf{d}_f = \mathbf{d}_s. \tag{6}$$

Furthermore, the tractions of the two domains at the interface are in equilibrium, i.e.

$$\boldsymbol{\sigma}_f \cdot \mathbf{n}_f + \boldsymbol{\sigma}_s \cdot \mathbf{n}_s = \mathbf{0}, \tag{7}$$

where $\boldsymbol{\sigma}$ denotes stress, $\mathbf{n}$ denotes the unit outward normal vector at the boundary; subscripts 'f' and 's' represent the fluid and solid domains, respectively. At the interface, $\mathbf{n}_f + \mathbf{n}_s = \mathbf{0}$.

2.4.4. Numerical method

FSI simulations were conducted using the software ADINA 9.3.0 installed in a workstation with Intel Xeon CPU (E5-1960 v4 @ 3.20 GHz with 8 cores) and 128 GB RAM. The fluid domain was modeled by the Flow-Condition-Based-Interpolation (FCBI) 4-node tetrahedral elements. The solid domain was modeled mainly by the 4-node with a small portion of 3-node 3D-elements. ADINA provides the one-way and two-way FSI couplings. As the former does not consider the effect of structural deformation on the fluid flow, the two-way coupling mode was selected. The linearized matrix equation was solved by the direct or non-iterative solution method. A fully implicit Euler scheme with 1 ms step was used in the time stepping. The time step was chosen by balancing the computing time and the convergence with respect to the time step. For instance, the maximum effective stresses of Patient A predicted by using time steps of 2, 1 and 0.5 ms are 531.6, 495.3 and 492.7 kPa, respectively. Meanwhile, the computing times over one cardiac cycle are 6.7, 13.1 and 25.9 h, respectively. Since the predictions based on 1 and 0.5 ms are very close, 1 ms was chosen to save computing time. The relative force tolerance and displacement tolerance between two successive iterations were set to 0.01 or 1% as the convergence criteria.

2.4.5. Mesh

Mesh independence tests were carried out for all models involved and results were presented in Table 2. Generally, computations were repeated for mesh grids of increasing resolution until the maximum wall effective stress remained practically unchanged when a finer mesh was employed. In the current study, meshes with 0.30 mm maximum element edge length were specified for the models of Patients A, B and C (before and after the scaling scheme). Meshes with a smaller maximum element edge length of 0.20 mm was adopted for the model of Patient D (before and after scaling). Final meshes of the fluid domain adopted for one sidewall aneurysm (Patient A) and one bifurcation aneurysm (Patient C) before and after scaling can be seen in Figure 4. The computing time over three cardiac cycles for all models were summarized in Table 3. As the scaled models are physically larger and contain more elements, they consume more computing time than the un-scaled models. For example, the computing time of Patient A under normal pressure condition after scaling is 46.2 h while that before scaling is 39.3 h.

Table 2. Mesh independence test.

The maximum wall effective stress (kPa)				
		Maximum length of the mesh edge (mm)		
Models		0.35	0.30	0.25
Patient A	Before scaling	532.8	495.3	493.8
	After scaling	772.9	720.8	717.5
Patient B	Before scaling	302.3	286.5	283.9
	After scaling	659.5	628.1	622.4
Patient C	Before scaling	478.4	450.5	446.4
	After scaling	995.2	930.1	921.8
The maximum wall effective stress (kPa)				
		Maximum length of the mesh edge (mm)		
Model		0.25	0.20	0.15
Patient D	Before scaling	331.7	315.9	312.4
	After scaling	761.7	708.4	704.1

Table 3. The computing times for all models.

	Before scaling (hour)		After scaling (hour)	
Model	Normal pressure	Hypertension	Normal pressure	Hypertension
Patient A	39.3	40.7	46.2	48.7
Patient B	41.6	43.5	47.1	49.1
Patient C	40.2	41.4	46.6	48.1
Patient D	42.3	43.8	50.1	50.9

3. Results and discussions

To assess the rupture risk of aneurysms with higher AR and smaller t_w after scaling which mimics the aneurysm growth, hemodynamics parameters including flow pattern inside the aneurysm, *WSS* and the aneurysmal wall stress were analysed. The predictions become periodic after two cycles of blood flow and those of the third cycle would be reported.

3.1. The influence of scaling on hemodynamics

3.1.1. Flow pattern

For both sidewall aneurysms and bifurcation aneurysms, the flow patterns are not altered substantially when the models are scaled, i.e. before and after the increase in

AR and reduction of t_w (Figure 5). Blood flow enters the aneurysm at the distal neck region and leaves at the proximal neck region. A vortex is observed inside the aneurysm. This flow pattern agrees well with previous studies (Liou & Li, 2008). However, there is a notable reduction in flow speed inside the aneurysm as the AR increases (Figure 5). A possible explanation is that the ratio of the neck width to the aneurysm height becomes relatively smaller as the AR increases, thereby restricting flow from entering the aneurysm. This reduction in flow speed due to an increase in AR is more dramatic in bifurcation aneurysms, as the inlet vessel would lead to an almost direct fluid impingement on the aneurysm neck. For smaller AR, the neck provides enough room for the inflow jet. For larger AR, more blood flow is diverted to the daughter vessels, effectively offering a larger obstruction to the inflow jet. Previous clinical reports have associated higher AR with a larger rupture risk (Ujiie et al., 2001), a property which cannot be explained by the flow pattern alone. A more illuminating consideration is to investigate the *WSS* and the wall stress which are described in the subsequent sections.

3.1.2. Wall shear stress (WSS) on aneurysmal wall

WSS is the fluid friction acting on the aneurysmal wall. For low *WSS*, rupture risk is aggravated and long-term damage is inflicted due to abnormal alignment of endothelial cells (Irace et al., 2004; Sho et al., 2001; Shojima et al., 2004). Instantaneous distribution of *WSS* at peak systole of all patient models follows an analogus pattern, with lower (higher) *WSS* occuring at the aneurysm (parent vessel) wall region (Figure 6), suggesting that the aneurysmal wall may be more vulnerable to long-term damage than normal vessel wall. Time averaged *WSS* (*TAWSS*) is a commonly used hemodynamic parameter in assessing the aneurysm rupture risk and is defined as

$$TAWSS = \frac{1}{T}\int_0^T |\vec{\tau}_w|\,\mathrm{d}t, \tag{8}$$

where $\vec{\tau}_w$ is the *WSS* and T represents the period of the cardiac cycle. *TAWSS* of three control points in the aneurysmal region (namely proximal neck, distal neck and dome) for each patient-specific model were investigated.

For all the four patient-specific models, the *WSS* is reduced when the aneurysm attains a higher AR and a smaller t_w after scaling during the whole cardiac cycle (Figure 7). Take Patient A as an example to show the results of the sidewall aneurysms. At a typical point on the proximal neck where the flow impinges, the *WSS* before (AR = 1.5, t_w = 0.3 mm) and after (AR = 1.8, t_w = 0.15 mm) scaling are in the range of 1 to 5 Pa and 0 to 3 Pa within a cardiac cycle whilst the *TAWSS* are 1.94 and 1.14 Pa, respectively. Both *WSS* and *TAWSS* are reduced considerably after the growth process. *WSS* and *TAWSS* also decrease in the distal neck and dome regions. For instance, the *TAWSS* at a typical point on the dome reduces from 0.21 to 0.18 Pa after growth (Table 4). For bifurcation aneurysms, similar reductions are observed. For example, the *WSS* for Patient C at the distal neck ranges from 0 to 2.5 Pa within a cardiac cycle, giving a *TAWSS* of 0.97 Pa before growth. After growth, the *WSS* ranges from 0 to 1.6 Pa and the *TAWSS* is 0.67 Pa. The

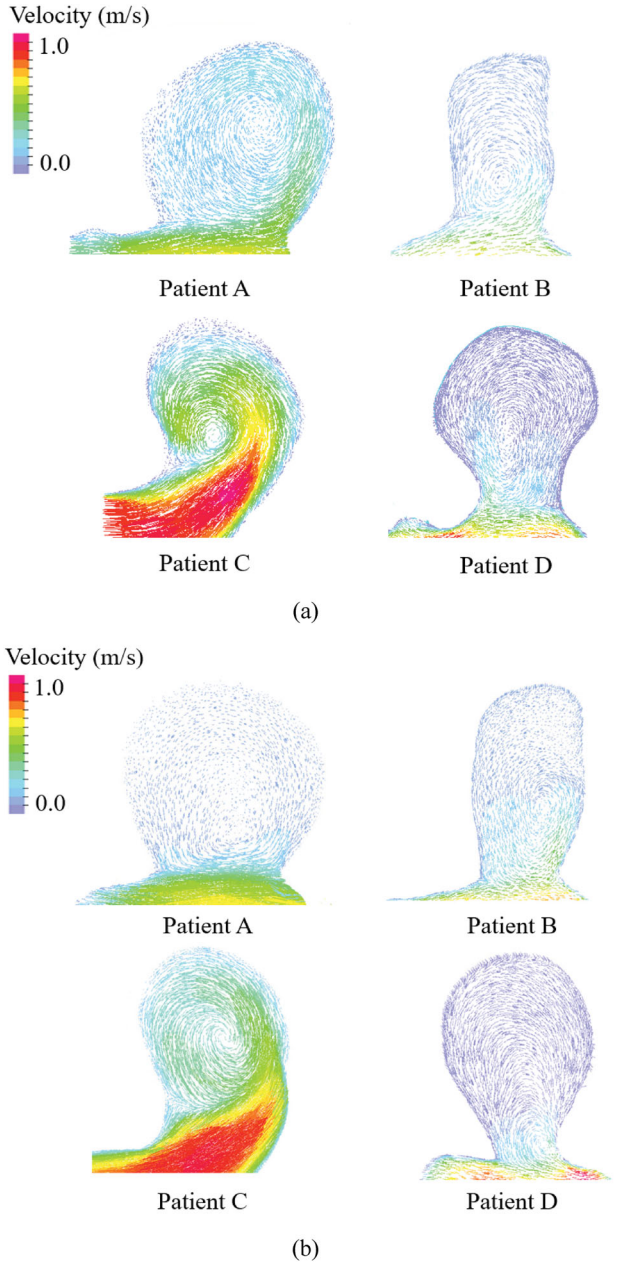

Figure 5. The velocity fields at peak systole: (a) before scaling, (b) after scaling.

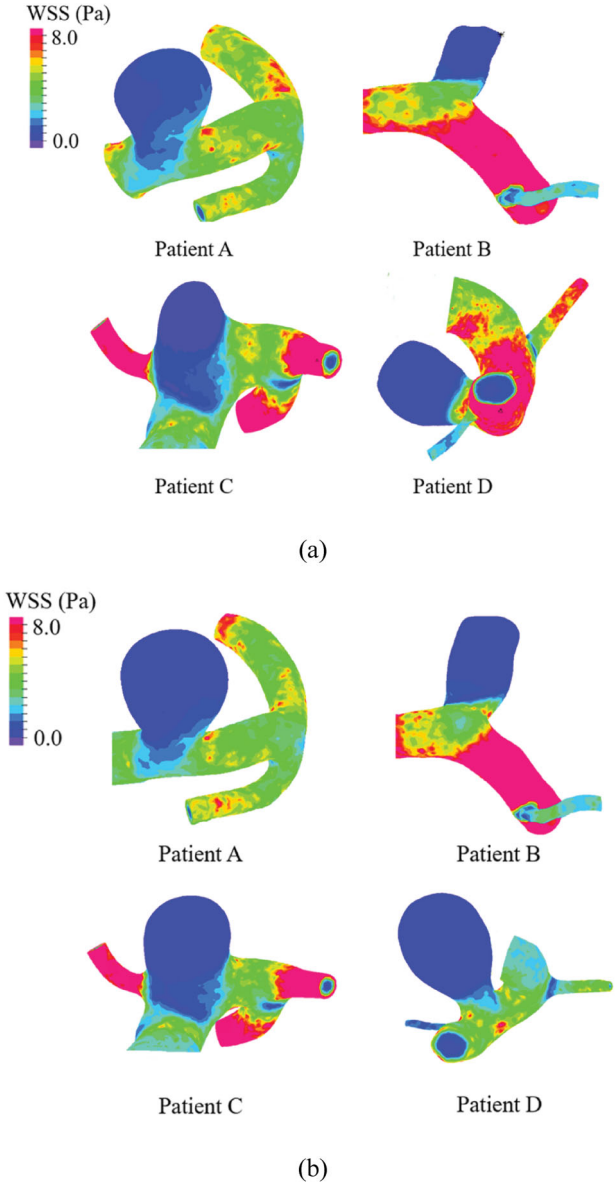

Figure 6. Instantaneous *WSS* distribution at peak systole: (a) before scaling, (b) after scaling.

variation of *WSS* within a cardiac cycle and the *TAWSS* for other models can be observed in Figure 7 and Table 4 respectively.

3.2. The influence of scaling on wall stresses

As mentioned in Section 2.2, AR would increase and t_w would reduce during the growth phase of the aneurysm which is mimicked by our scaling method. The influence of this scaling on the wall stresses will now be studied. Since the actual values of t_w and their variations are not known, the current study focuses on the hemodynamic features and the changes in wall stresses when t_w has dropped to 0.15 mm due to the growth process. Compared with the reported 0.05 mm lowest post-rupture t_w, (Abruzzo et al., 1998), the present 0.15 mm thickness is an intermediate thickness adopted to study the effect of scaling which leads to AR increase and wall thinning.

3.2.1. Effective stress (von Mises stress)

Predictions of solid material failures are often based on the effective stress. In recent years, it has been adopted as a criterion for predicting the aneurysm rupture risk (Volokh, 2008). The effective stress

$$\sigma_e = \sqrt{\frac{(\sigma_{xx}-\sigma_{yy})^2+(\sigma_{xx}-\sigma_{zz})^2+(\sigma_{yy}-\sigma_{zz})^2+6(\sigma_{xy}^2+\sigma_{xz}^2+\sigma_{yz}^2)}{2}}, \tag{9}$$

is a scalar quantity defined using the Cauchy or true stress components σ_{ij}s. In the present context, rupture may occur when the effective stress of the wall exceeds the strength of the aneurysmal wall (Isaksen et al., 2008). However, the actual strength undoubtedly varies from patient to patient. Moreover, AR often increases and t_w reduces when the aneurysm grows (Suzuki & Ohara, 1978; Torii et al., 2010). Consequently, the current study focuses on how the effective stress would change as the aneurysm is scaled up in which AR increases and t_w decreases.

The abrupt geometric change at the neck region always induces there the highest stress (Figure 8). On the other hand, IA ruptures often occur at the aneurysm domes. Here, both the maximum effective stresses at the neck region and the dome were captured and reported (Table 5). Furthermore, the maximum σ_e increases for all models after scaling, suggesting that an aneurysm with a higher AR and lower t_w poses a greater rupture risk. For sidewall aneurysms, the maximum σ_e at the neck for Patient A increases from 495.3 to 720.8 kPa after scaling (AR = 1.5 & t_w = 0.3 mm to AR = 1.8 & t_w = 0.15 mm), while the corresponding trend at the dome is an increase from 60.0 to 391.4 kPa. The increase in the maximum σ_e at the dome for Patient B due to model growth is 105 kPa (from 45.6 to 150.6 kPa), while the corresponding value at the neck is 341.6 kPa (from 286.5 to 628.1 kPa). For bifurcation aneurysms, the maximum σ_e at the dome for Patient C increases from 55.6 to 365.0 kPa after scaling (AR = 1.2 & t_w = 0.3 mm to AR = 1.5 & t_w = 0.15 mm), while the maximum σ_e at the neck increases from 450.5 to 930.1 kPa. The maximum σ_e at the dome for Patient D increases by 385.9 kPa from 42.9 to 428.8 kPa, while the corresponding trend at the neck is 392.5 kPa from 315.9 to 708.4 kPa. Consequently, both sidewall and bifurcation aneurysms are

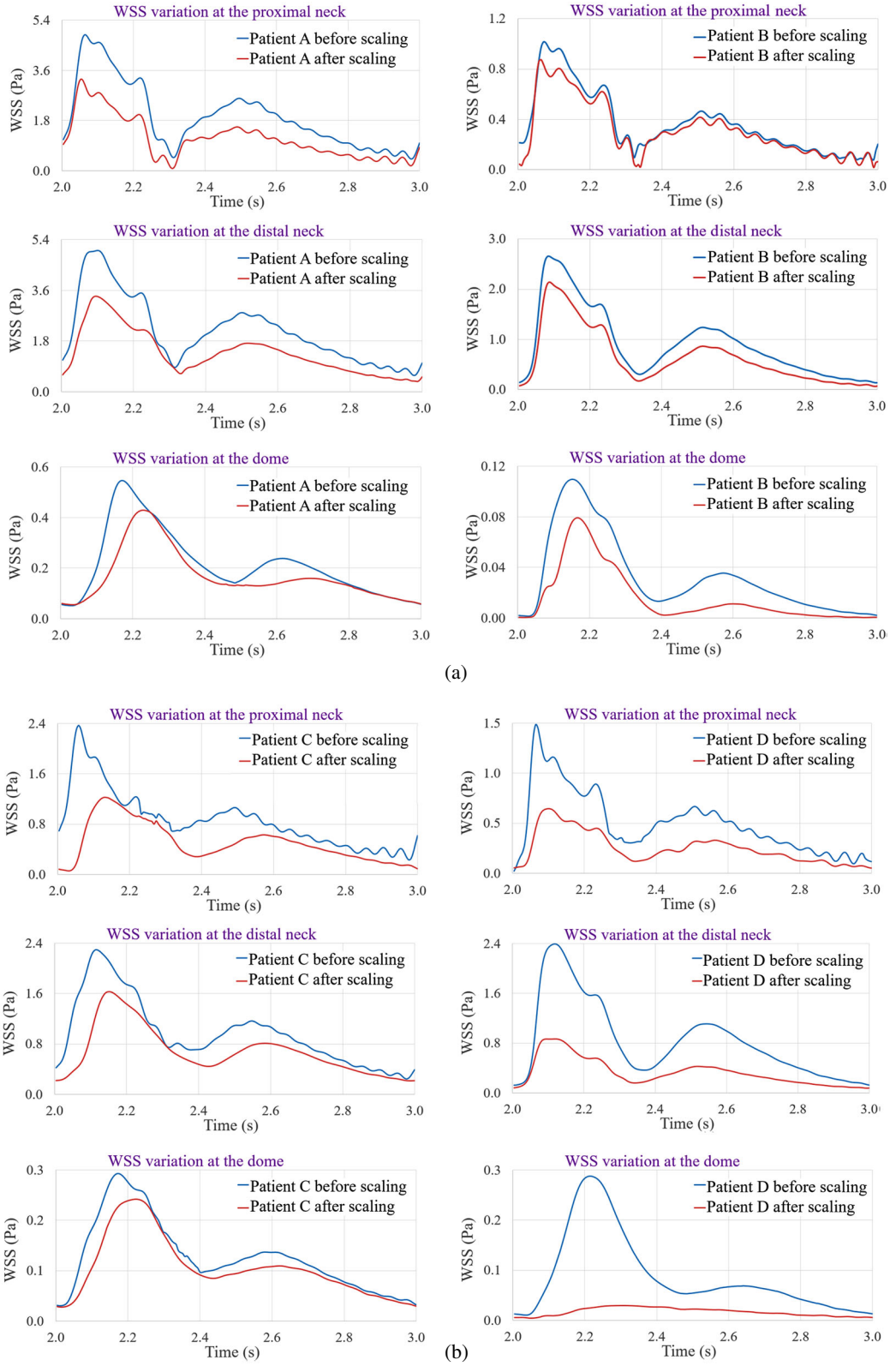

Figure 7. *WSS* variation over a cardiac cycle. (a) Sidewall aneurysms, (b) Bifurcation aneurysms.

Table 4. The influence of scaling on *TAWSS* under normal pressure condition (120 / 80 mmHg).

	TAWSS (Pa)							
	Before scaling				After scaling			
Model	AR	Proximal neck	Distal neck	Dome	AR	Proximal neck	Distal neck	Dome
Patient A	1.5	1.94	2.16	0.21	1.8	1.14	1.35	0.18
Patient B	1.9	0.36	0.91	0.03	2.3	0.31	0.47	0.02
Patient C	1.2	0.71	0.97	0.12	1.5	0.56	0.67	0.11
Patient D	2.2	0.49	0.83	0.09	2.6	0.25	0.32	0.02

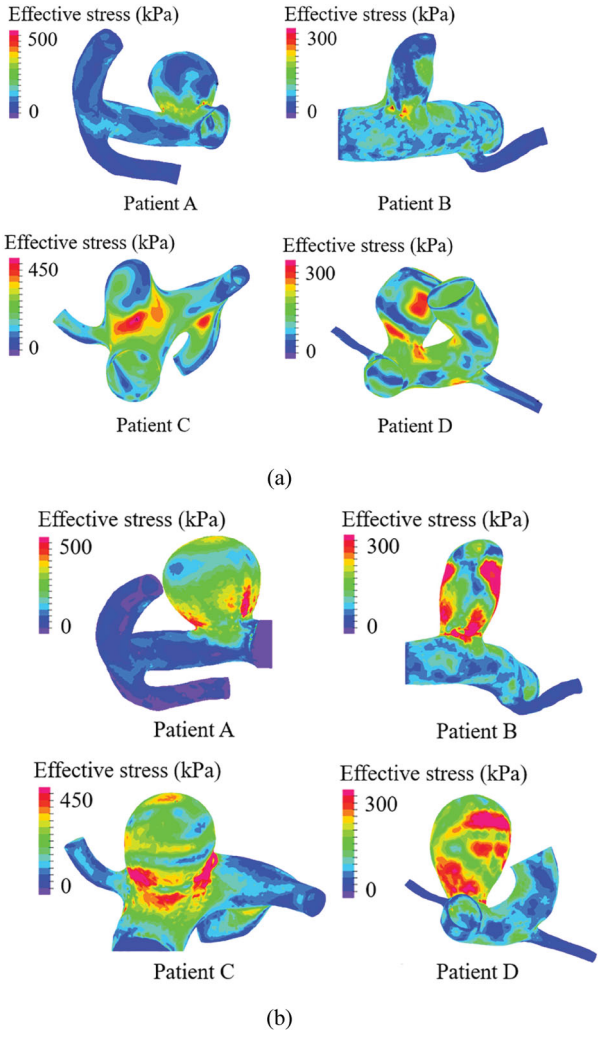

Figure 8. The effective stress distribution of all models at peak systole: (a) before scaling, (b) after scaling.

conjectured to suffer a higher risk of rupture as the aneurysm is scaled to the state with a higher AR.

3.2.2. First principal stress

Values of stress components change with the coordinate axes. The first principal stress σ_1 is the largest normal stress one can obtain by varying the directions of the coordinate axes. Similar to the effective stress, σ_1 is a commonly used stress parameter in material failure predictions. The maximum first principal stresses before and after scaling are summarized in Table 6. Their magnitudes and percentage changes due to scaling are consistent with the qualitative trend for the effective stresses presented in the last paragraph. In other words, the rupture assessments based on both the effective and first principal stresses lead to the similar outcomes.

Table 5. The influence of scaling on the effective stress.

	Maximum σ_e at aneurysmal neck (kPa)		Maximum σ_e at aneurysmal dome (kPa)	
Model	Before scaling	After scaling	Before scaling	After scaling
Patient A	495.3	721.8	60.0	391.4
Patient B	286.5	628.1	45.6	150.6
Patient C	450.5	930.1	55.6	365.0
Patient D	315.9	708.4	42.9	428.8

Table 6. The influence of scaling on the first principal stress.

	Maximum σ_1 at neck (kPa)		Maximum σ_1 at dome (kPa)	
Model	Before scaling	After scaling	Before scaling	After scaling
Patient A	534.1	773.9	66.3	389.9
Patient B	305.5	642.8	44.6	174.2
Patient C	504.4	1046.9	59.0	391.5
Patient D	366.2	726.0	45.0	430.9

3.3. The influence of scaling on the wall displacement

After scaling, the maximum displacements at systole for all models increase (Figure 9). Before scaling, such maximum displacements are 0.758, 0.432, 1.477 and 0.996 mm for Patients A, B, C and D, respectively. After scaling, the corresponding values are 1.403, 0.801, 1.946 and 1.478 mm, respectively. The maximum displacements for Patient A, C and D always occur at the aneurysmal dome where rupture usually occurs clinically. However, the maximum displacement for Patient B is found at the region near to but not at the dome, a variation probably due to different morphology.

3.4. The influence of hypertension

High blood pressure is believed to play an important role in the development, growth and rupture of aneurysms

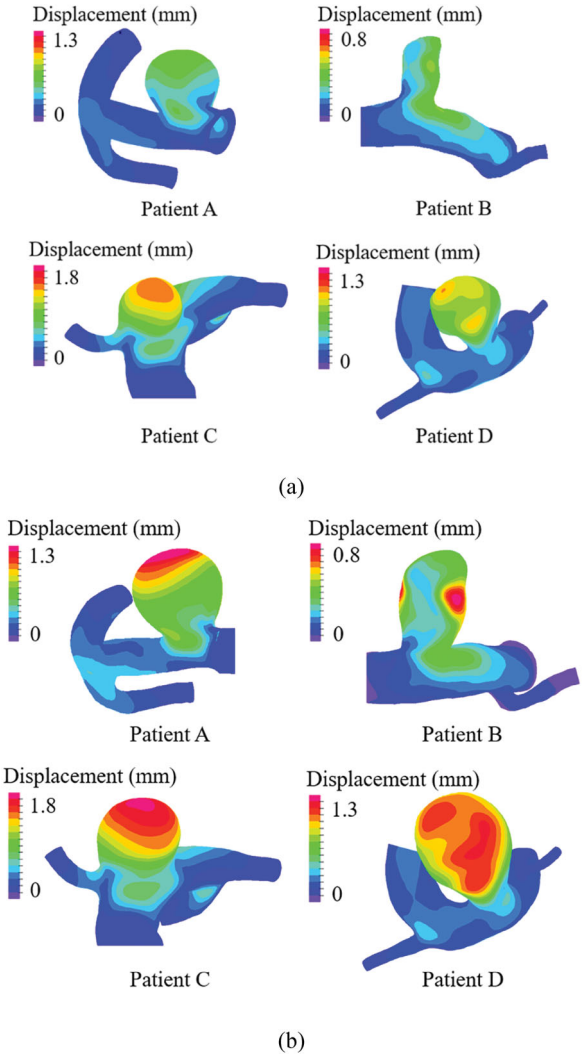

Figure 9. The displacement distribution of all models at peak systole: (a) before scaling, (b) after scaling.

(Brisman, Song, & Newell, 2006; Lasheras, 2007). The current study will also investigate the effect of hypertension.

3.4.1. The influence of hypertension and AR on the wall stresses

The wall stresses for all models before and after the aneurysm growth process were studied for both normal blood pressure (120/80 mmHg) and hypertension (160/100 mmHg) conditions. The inlet volume flow rate under hypertension condition was the same as that for the normal pressure condition (Figure 3). There are majorly three reasons why we think it is a reasonable assumption. Firstly, the literature did not give a well-defined algorithm for computing the modified volumetric blood flow rate for hypertension condition (especially in the range of 160/100 mmHg which is used in the current study). And clinically it is impossible or unethical

Table 7. The influence of scaling and hypertension on the maximum σ_e at the dome.

Model		The maximum σ_e at the dome (kPa)		
		Normal pressure	Hypertension	$\Delta\sigma_e$
Patient A	Before scaling	60.0	81.1	21.1
	After scaling	391.4	522.2	130.6
Patient B	Before scaling	45.6	62.1	16.5
	After scaling	150.6	205.7	55.1
Patient C	Before scaling	55.6	74.0	18.4
	After scaling	365.0	489.2	124.2
Patient D	Before scaling	42.9	59.4	16.5
	After scaling	428.8	616.7	187.9

where $\Delta\sigma_e = (\sigma_e)_{\text{underhypertension}} - (\sigma_e)_{\text{undernormalpressure}}$.

Table 8. The influence of scaling and hypertension on the maximum σ_1 at the dome.

Model		The maximum σ_1 at the dome (kPa)		
		Normal Pressure	Hypertension	$\Delta\sigma_1$
Patient A	Before scaling	66.3	89.4	22.8
	After scaling	389.9	546.5	156.4
Patient B	Before scaling	44.6	60.4	15.8
	After scaling	174.2	236.7	62.5
Patient C	Before scaling	59.0	79.0	20.0
	After scaling	391.5	525.9	134.4
Patient D	Before scaling	45.0	62.2	17.2
	After scaling	430.9	635.9	205.0

where $\Delta\sigma_1 = (\sigma_1)u_{\text{nderhypertension}} - (\sigma_1)_{\text{undernormalpressure}}$.

to measure changing pressure waveforms by inducing hypertension this way. Secondly, the previous papers in the literature which covered the issue of hypertension frequently used the same flow rate for both normal pressure and hypertension conditions (Lee et al., 2013; Torii et al., 2007; Torii, Oshima, Kobayashi, Takagi, & Tezduyar, 2006; Valencia & Torres, 2017). Thirdly, the current study aims to study how the wall stresses will change when the pressure condition changes from normal pressure to hypertension. The underlying assumption is that the aneurysm may rupture when its wall stress exceeds a threshold of material property. This threshold or yield stress may vary for different patients. From our computational results, the wall stresses are significantly affected by the blood pressure, but the influence of the flow rate is very small. With all these considerations, we think that using the same flow rate for both normal pressure and hypertension would still be a reasonable assumption.

The results of the maximum σ_e and σ_1 at the dome, where the aneurysm is more vulnerable to rupture, were compared and summarized in Tables 7 and 8. Not surprisingly, the maximum wall stresses (including σ_e and σ_1) for all models will increase as the blood pressure changes from 120/80 to 160/100 mmHg. Moreover, this increase of the wall stresses at the aneurysmal dome for the models after scaling is much more profound than those before growth with a lower AR.

Table 9. The influence of hypertension on *TAWSS* before scaling.

	TAWSS (Pa) before scaling					
	Normal pressure			Hypertension		
Model	Proximal neck	Distal neck	Dome	Proximal neck	Distal neck	Dome
Patient A	1.94	2.16	0.21	1.88	2.08	0.21
Patient B	0.36	0.91	0.03	0.35	0.89	0.03
Patient C	0.71	0.97	0.12	0.61	0.77	0.12
Patient D	0.49	0.83	0.09	0.41	0.64	0.09

Table 10. The influence of scaling and hypertension on *TAWSS*.

	TAWSS (Pa) under hypertension condition					
	Before scaling			After scaling		
Model	Proximal neck	Distal neck	Dome	Proximal neck	Distal neck	Dome
Patient A	1.88	2.08	0.21	0.86	1.19	0.14
Patient B	0.35	0.89	0.03	0.30	0.47	0.02
Patient C	0.61	0.77	0.12	0.54	0.66	0.11
Patient D	0.41	0.64	0.09	0.24	0.32	0.02

For sidewall aneurysms, taking Patient A for instance, the increase of the maximum σ_e at the dome for the model before scaling due to hypertension is 21.1 kPa, however, this increase is much larger (130.6 kPa) for the model after scaling. The maximum σ_1 at the dome for Patient A after scaling increases by 156.4 kPa due to hypertension, compared to 22.8 kPa for the model before scaling. For bifurcation aneurysms, taking Patient C for example, the maximum σ_e at the dome for the model after scaling increases by 124.2 kPa because of hypertension, in contrast, the corresponding increase for the model before scaling is just 18.4 kPa The increase of the maximum σ_1 for Patient C after scaling due to hypertension is 134.4 kPa, compared to only 20.0 kPa for the model before scaling. Consequently, the models with a higher AR and lower t_w after scaling suffer greater rupture risk compared with the ones with a lower AR and higher t_w before scaling in hypertension states.

3.4.2. The influence of hypertension on TAWSS

In Section 3.1.2, the influence of AR and t_w on the *TAWSS* is studied. Based on the models before scaling, Table 9 presents the changes in *TAWSS* for all models due to hypertension. Our results showed that the *TAWSS* for all models would generally decrease when the pressure is changed from a normal to a hypertension range (Table 9). The reason is that the velocity gradient would decrease due to the dilatation of the vessel and aneurysmal wall caused by hypertension. As examples, the *TAWSS* at the proximal (distal) neck for Patient C reduces from 0.71 (0.97) to 0.61 (0.77) Pa when the blood pressure is changed from a normal value to hypertension. The *TAWSS* at the proximal neck under hypertension for Patient D is 0.41 Pa, which is lower than that (0.49 Pa) under the condition of normal pressure. However, the *TAWSS* at the dome for all models is not sensitive to the change in pressure waveform probably due to the rather stagnant flow in the region.

Next, *TAWSS* under hypertension before and after scaling were studied. Results are summarized in Table 10. It is found that the *TAWSS* for all the models after scaling are lowered, which is similar to the situation of normal pressure. Taking the sidewall aneurysms as example, the *TAWSS*s of Patient B at the proximal (distal) neck is 0.35 (0.89) and 0.30 (0.47) Pa before and after scaling. The *TAWSS*s at the dome for the same patient before and after scaling are 0.03 and 0.02 Pa, respectively.

For bifurcation aneurysms, the *TAWSS*s of Patient D at the proximal (distal) neck are 0.41 (0.64) and 0.24 (0.32) Pa before and after scaling. On the other hand, the *TAWSS*s at the dome for the same patient are 0.09 and 0.02 Pa, respectively. Thus, aneurysms with higher AR and lower t_w after scaling would experience long-term low *WSS* effect under the condition of hypertension, with the implication that they are at a greater risk of rupture.

3.5. The influence of AR increase alone

In the scaling procedure to mimic aneurysm growth, AR is increased and t_w is reduced to 0.15 mm. As a control experiment, it would be instructive to examine the variation in wall stress when AR is increased but t_w is kept intact at 0.3 mm.

The results show that the maximum σ_e both at the neck and the dome increases for all the four models as the AR increases. For example, the maximum σ_e at the neck (dome) for Patient C increases from 450.5 (55.6) to 604.7 (198.7) kPa. The results of the other models exhibit

Table 11. The influence of scaling but keeping t_w intact on the effective stress.

	Maximum σ_e at aneurysmal neck (kPa)		Maximum σ_e at aneurysmal dome (kPa)	
Model	Before scaling	After scaling but keeping t_w at 0.30 mm	Before scaling	After scaling but keeping t_w at 0.30 mm
Patient A	495.3	515.9	60.0	226.8
Patient B	286.5	365.3	45.6	104.7
Patient C	450.5	604.7	55.6	198.7
Patient D	315.9	445.4	42.9	316.8

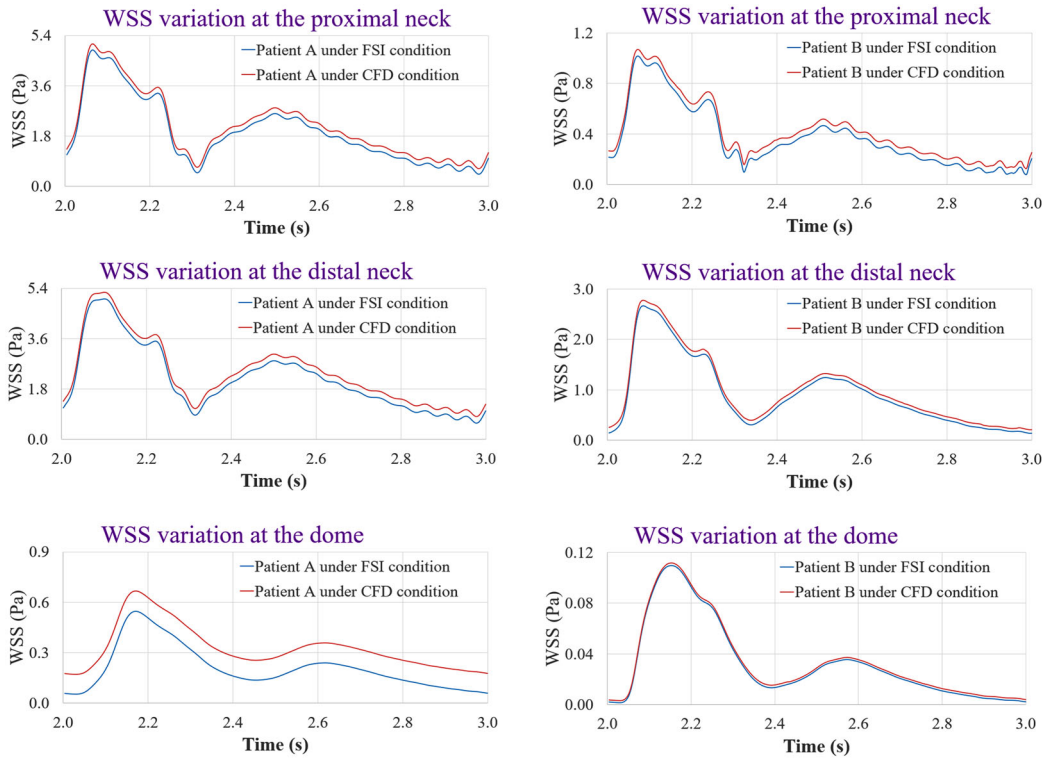

(a)

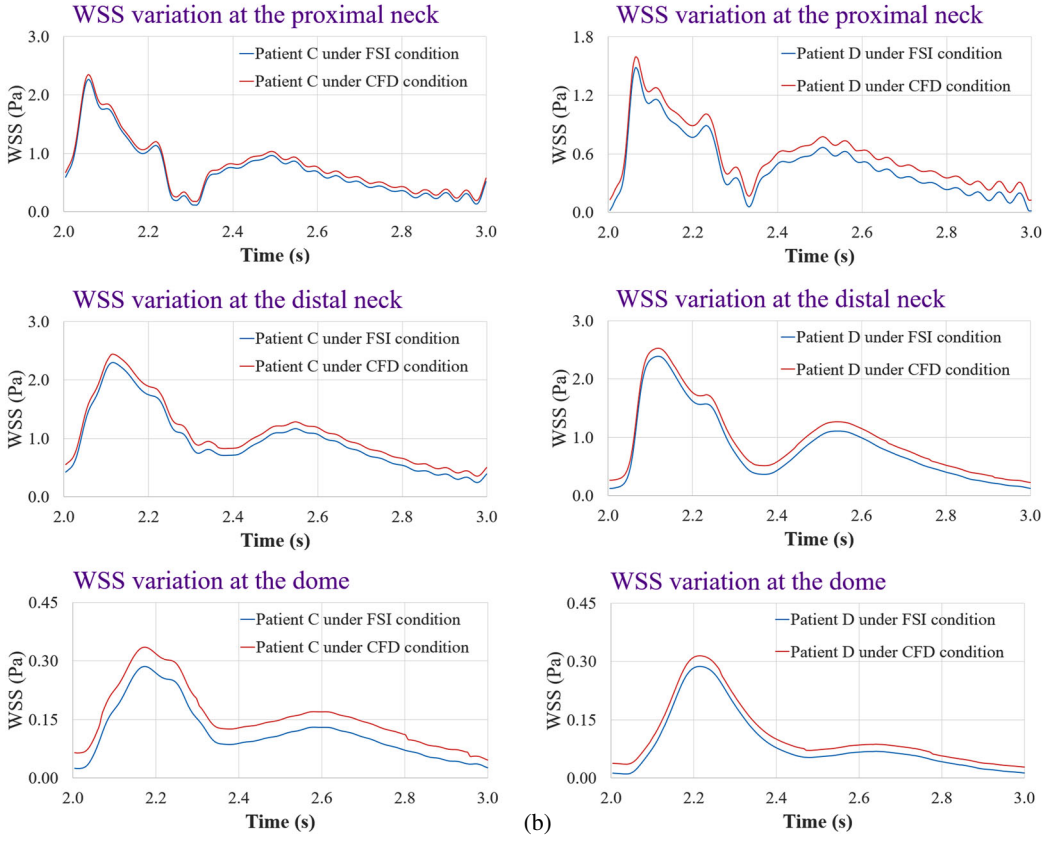

(b)

Figure 10. The comparison of *WSS* variation over one cardiac cycle between FSI and CFD. (a) Sidewall aneurysms, (b) Bifurcation aneurysms.

the same trend and are summarized in Table 11. Models with a higher AR thus suffer from higher σ_e, posing a higher rupture risk.

4. Conclusions

From clinical observations over the years, aneurysms with larger aspect ratios (ARs) have been associated with a higher rupture risk. The present study should be valuable in providing quantitative data and trends in constituting relations among AR increase, wall thickness (t_w) reduction due to aneurysm growth, hemodynamic features of the fluid medium, as well as the effective and principal stresses in the aneurysm wall. By utilizing FSI simulations on four patient-specific models before and after scaling which mimics the growth process, fluid domains with long-term low wall shear stress (*WSS*) effect are revealed. Moreover, the wall stresses at the aneurysm dome (the region more vulnerable to rupture) will increase notably as the AR increases and the t_w reduces due to aneurysm growth. Furthermore, this phenomenon is particularly profound in hypertension condition, justifying the clinical need to avoid scenarios of high blood pressure for such patients.

Predictions from computational fluid dynamics (CFD), with the assumption of rigid walls, and fluid-structure interaction (FSI) on patient-specific models have been compared. The flow patterns between the two approaches are very similar while the fluid shear stresses obtained from FSI are smaller than those from CFD simulations due to the dilation of the aneurysm (Figure 10). For example, the *TAWSS*s at the proximal neck for Patient A, B, C and D before scaling based on CFD are 2.15, 0.42, 0.78 and 0.57 Pa, while the corresponding values based on FSI are 1.94, 0.36, 0.71 and 0.49 Pa, respectively. Besides, the FSI could provide the response of the solid domain for the coupled system, which could not be obtained by CFD alone. Advantages of the FSI scheme are thus illustrated.

The merits of performing FSI include its non-invasive nature and relatively low cost. However, there are some limitations in the current study. Firstly, blood is modeled as a Newtonian fluid, and non-Newtonian models should be incorporated in the future to account for the shear thinning behavior. Secondly, the thickness of the aneurysm sac and the vessel walls is assumed to be uniform, arising from the limitation in the resolution of available imaging technology at our clinical centers. Despite these limitations, current effort should be valuable in providing quantitative data and trends in constituting relations between aneurysm growth and its rupture risk. In the future, further patient studies will be collected to provide more substantive data sets.

Disclosure statement

No potential conflict of interest was reported by the authors.

Funding

Partial financial support has been provided by the Innovation and Technology Fund [grant number ITS/150/15] of the Government of the Hong Kong Special Administrative Region.

References

Abruzzo, T., Shengelaia, G., Dawson, R., Owens, D., Cawley, C., & Gravanis, M. (1998). Histologic and morphologic comparison of experimental aneurysms with human intracranial aneurysms. *American Journal of Neuroradiology*, *19*(7), 1309–1314.

Ahmed, S., Šutalo, I. D., Kavnoudias, H., & Madan, A. (2011). Numerical investigation of hemodynamics of lateral cerebral aneurysm following coil embolization. *Engineering Applications of Computational Fluid Mechanics*, *5*(3), 329–340. doi:10.1080/19942060.2011.11015375

Badia, S., Nobile, F., & Vergara, C. (2009). Robin-robin preconditioned krylov methods for fluid–structure interaction problems. *Computer Methods in Applied Mechanics and Engineering*, *198*, 2768–2784. doi:10.1016/j.cma.2009.04.004

Bazilevs, Y., Hsu, M. C., Zhang, Y., Wang, W., Liang, X., Kvamsdal, T., ... Isaksen, J. G. (2010). A fully-coupled fluid–structure interaction simulation of cerebral aneurysms. *Computational Mechanics*, *46*(1), 3–16. doi:10.1007/s00466-009-0421-4

Belytscho, T., Liu, W. K., Moran, B., & Elkhodary, K. (2014). *Nonlinear finite elements for continua and structures* (2nd ed.). Chichester, UK: Wiley.

Berg, P., Roloff, C., Beuing, O., Voss, S., Sugiyama, S., Aristokleous, N., ... Janiga, G. (2015). The computational fluid dynamics rupture challenge 2013–phase II: Variability of hemodynamic simulations in two intracranial aneurysms. *Journal of Biomechanical Engineering*, *137*(12), 121008. doi:10.1115/1.4031794

Brisman, J. L., Song, J. K., & Newell, D. W. (2006). Cerebral aneurysms. *New England Journal of Medicine*, *355*(9), 928–939. doi:10.1056/NEJMra052760

Ford, M. D., Lee, S. W., Lownie, S. P., Holdsworth, D. W., & Steinman, D. A. (2008a). On the effect of parent-aneurysm angle on flow patterns in basilar tip aneurysms: Towards a surrogate geometric marker of intra-aneurismal hemodynamics. *Journal of Biomechanics*, *41*(2), 241–248. doi:10.1016/j.jbiomech.2007.09.032

Ford, M. D., Nikolov, H. N., Milner, J. S., Lownie, S. P., Demont, E. M., Kalata, W., ... Steinman, D. A. (2008b). PIV-measured versus CFD-predicted flow dynamics in anatomically realistic cerebral aneurysm models. Journal of Biomechanical Engineering. *Transactions of the ASME*, *130*(2), 021015. doi:10.1115/1.2900724

Hoi, Y., Wasserman, B. A., Lakatta, E. G., & Steinman, D. A. (2010). Effect of common carotid artery inlet length on normal carotid bifurcation hemodynamics. *Journal of Biomechanical Engineering*, *132*(12), 121008. doi:10.1115/1.4002800

Humphrey, J. D., & Taylor, C. A. (2008). Intracranial and abdominal aortic aneurysms: Similarities, differences, and

need for a new class of computational models. *Annual Review of Biomedical Engineering*, *10*, 221–246. doi:10.1146/annurev.bioeng.10.061807.160439

Inthavong, K., Wen, J., Tu, J., & Tian, Z. (2009). From CT scans to CFD modelling – fluid and heat transfer in a realistic human nasal cavity. *Engineering Applications of Computational Fluid Mechanics*, *3*(3), 321–335. doi:10.1080/19942060.2009.11015274

Irace, C., Cortese, C., Fiaschi, E., Carallo, C., Farinaro, E., & Gnasso, A. (2004). Wall shear stress is associated with intima-media thickness and carotid atherosclerosis in subjects at low coronary heart disease risk. *Stroke*, *35*(2), 464–468. doi:10.1161/01.STR.0000111597.34179.47

Isaksen, J. G., Bazilevs, Y., Kvamsdal, T., Zhang, Y., Kaspersen, J. H., Waterloo, K., ... Ingebrigtsen, T. (2008). Determination of wall tension in cerebral artery aneurysms by numerical simulation. *Stroke*, *39*(12), 3172–3178. doi:10.1161/STROKEAHA.107.503698

Kroon, M. (2011). Simulation of cerebral aneurysm growth and prediction of evolving rupture risk. *Modelling and Simulation in Engineering*, *2011*(10), 1155–1165. doi:10.1155/2011/289523

Ku, J. P., Elkins, C. J., & Taylor, C. A. (2005). Comparison of CFD and MRI flow and velocities in an in vitro large artery bypass graft model. *Annals of Biomedical Engineering*, *33*(3), 257–269. doi:10.1007/s10439-005-1729-7

Ku, D. N., Giddens, D. P., Zarins, C. K., & Glagov, S. (1985). Pulsatile flow and atherosclerosis in the human carotid bifurcation: Positive correlation between plaque location and low oscillating shear stress. Arteriosclerosis. *Thrombosis, and Vascular Biology*, *5*(3), 293–302. doi:10.1161/01.ATV.5.3.293

Lai, S. S. M., Tang, A. Y. S., Tsang, A. C. O., Leung, G. K. K., Yu, A. C. H., & Chow, K. W. (2016). A joint computational-experimental study of intracranial aneurysms: Importance of the aspect ratio. *Journal of Hydrodynamics*, *28*(3), 462–472. doi:10.1016/S1001-6058(16)60650-9

Lasheras, J. C. (2007). The biomechanics of arterial aneurysms. *Annual Review of Fluid Mechanics*, *39*, 293–319. doi:10.1146/annurev.fluid.39.050905.110128

Lee, C. J., Zhang, Y., Takao, H., Murayama, Y., & Qian, Y. (2013). A fluid-structure interaction study using patient-specific ruptured and unruptured aneurysm: The effect of aneurysm morphology, hypertension and elasticity. *Journal of Biomechanics*, *46*(14), 2402–2410. doi:10.1016/j.jbiomech.2013.07.016

Liou, T. M., & Li, Y. C. (2008). Effects of stent porosity on hemodynamics in a sidewall aneurysm model. *Journal of Biomechanics*, *41*(6), 1174–1183. doi:10.1016/j.jbiomech.2008.01.025

Long, Y. L., Zhong, J. R., Yu, H. Y., Yan, H. G., Zhuo, Z. Z., Meng, Q. Q., ... Li, H. Y. (2015). A scaling aneurysm model-based approach to assessing the role of flow pattern and energy loss in aneurysm rupture prediction. *Journal of Translational Medicine*, *13*, 311. doi:10.1186/s12967-015-0673-z

McGarry, M., Hitt, D. L., & Harris, T. R. (2008). Leakage rates from a punctured vessel under pulsatile flow conditions. *Engineering Applications of Computational Fluid Mechanics*, *2*(3), 275–283. doi:10.1080/19942060.2008.11015228

Nair, P., Chong, B. W., Indahlastari, A., Ryan, J., Workman, C., Haithem, B. M., ... Frakes, D. (2016). Hemodynamic characterization of geometric cerebral aneurysm templates treated with embolic coils. *Journal of Biomechanical Engineering*, *138*(2), 021011. doi:10.1115/1.4032046

Perktold, K., Kenner, T., Hilbert, D., Spork, B., & Florian, H. (1988). Numerical blood flow analysis: Arterial bifurcation with a saccular aneurysm. *Basic Research in Cardiology*, *83*(1), 24–31. doi:10.1007/BF01907101

Rayz, V. L., Boussel, L., Acevedo-Bolton, G., Martin, A. J., Young, W. L., Lawton, M. T., ... Saloner, D. (2008). Numerical simulations of flow in cerebral aneurysms: Comparison of CFD results and in vivo MRI measurements. *Journal of Biomechanical Engineering*, *130*(5), 051011. doi:10.1115/1.2970056

Riley, W. A., Barnes, R. W., Evans, G. W., & Burke, G. L. (1992). Ultrasonic measurement of the elastic modulus of the common carotid artery. The atherosclerosis risk in communities (ARIC) study. *Stroke*, *23*(7), 952–956. doi:10.1161/01.STR.23.7.952

Sanchez, M., Ambard, D., Costalat, V., Mendez, S., Jourdan, F., & Nicoud, F. (2013). Biomechanical assessment of the individual risk of rupture of cerebral aneurysms: A proof of concept. *Annals of Biomedical Engineering*, *41*(1), 28–40. doi:10.1007/s10439-012-0632-2

Sforza, D. M., Putman, C. M., & Cebral, J. R. (2009). Hemodynamics of cerebral aneurysms. *Annual Review of Fluid Mechanics*, *41*, 91–107. doi:10.1146/annurev.fluid.40.111406.102126

Sho, E., Sho, M., Singh, T. M., Xu, C., Zarins, C. K., & Masuda, H. (2001). Blood flow decrease induces apoptosis of endothelial cells in previously dilated arteries resulting from chronic high blood flow. *Arteriosclerosis, Thrombosis, and Vascular Biology*, *21*(7), 1139–1145. doi:10.1161/hq0701.092118

Shojima, M., Oshima, M., Takagi, K., Torii, R., Hayakawa, M., Katada, K., ... Kirino, T. (2004). Magnitude and role of wall shear stress on cerebral aneurysm. *Stroke*, *35*(11), 2500–2505. doi:10.1161/01.STR.0000144648.89172.0f

Sussman, T., & Bathe, K. J. (2013). 3D-shell elements for structures in large strains. *Computers & Structures*, *122*, 2–12. doi:10.1016/j.compstruc.2012.12.018

Suzuki, J., & Ohara, H. (1978). Clinicopathological study of cerebral aneurysms. Origin, rupture, repair, and growth. *Journal of Neurosurgery*, *48*(4), 505–514. doi:10.3171/jns.1978.48.4.0505

Tang, A. Y. S., Chung, W. C., Liu, E. T. Y., Qu, J. Q., Tsang, A. C. O., Leung, G. K. K., ... Chow, K. W. (2015). Computational fluid dynamics study of bifurcation aneurysms treated with pipeline embolization device: Side branch diameter study. *Journal of Medical and Biological Engineering*, *35*(3), 293–304. doi:10.1007/s40846-015-0046-3

Tang, A. Y. S., Fan, Y., Cheng, S. W. K., & Chow, K. W. (2012). Biomechanical factors influencing type B thoracic aortic dissection: Computational fluid dynamics study. *Engineering Applications of Computational Fluid Mechanics*, *6*(4), 622–632. doi:10.1080/19942060.2012.11015447

Torii, R., Oshima, M., Kobayashi, T., Takagi, K., Tezduyar, T., & Masud, A. (2007). Numerical investigation of the effect of hypertensive blood pressure on cerebral aneurysm—dependence of the effect on the aneurysm shape. *International Journal for Numerical Methods in Fluids*, *54*(6-8), 995–1009. doi:10.1002/fld.1497

Torii, R., Oshima, M., Kobayashi, T., Takagi, K., & Tezduyar, T. (2006). Fluid–structure interaction modeling of aneurysmal conditions with high and normal blood pressures. *Computational Mechanics*, *38*(4), 482–490. doi:10.1007/s00466-006-0065-6

Torii, R., Oshima, M., Kobayashi, T., Takagi, K., & Tezduyar, T. (2010). Influence of wall thickness on fluid–structure interaction computations of cerebral aneurysms. *International Journal for Numerical Methods in Engineering*, *26*(3-4), 336–347. doi:10.1002/cnm.1289

Torii, R., Oshima, M., Kobayashi, T., Takagi, K., & Tezduyar, T. E. (2011). Influencing factors in image-based fluid–structure interaction computation of cerebral aneurysms. *International Journal for Numerical Methods in Fluids*, *65*(1-3), 324–340. doi:10.1002/fld.2448

Ujiie, H., Tamano, Y., Sasaki, K., & Hori, T. (2001). Is the aspect ratio a reliable index for predicting the rupture of a saccular aneurysm? *Neurosurgery*, *48*(3), 495–503. doi:10.1097/00006123-200103000-00007

Valencia, A., Burdiles, P., Ignat, M., Mura, J., Bravo, E., Rivera, R., & Sordo, J. (2013). Fluid structural analysis of human cerebral aneurysm using their own wall mechanical properties. *Computational and Mathematical Methods in Medicine*, *2013*, 293128. doi:10.1155/2013/293128

Valencia, A., Contente, A., Ignat, M., Mura, J., Bravo, E., Rivera, R., & Sordo, J. (2015). Mechanical test of human cerebral aneurysm specimens obtained from surgical clipping. *Journal of Mechanics in Medicine and Biology*, *15*(5), 1550075. doi:10.1142/S021951941550075X

Valencia, A., Ledermann, D., Rivera, R., Bravo, E., & Galvez, M. (2008). Blood flow dynamics and fluid-structure interaction in patient-specific bifurcating cerebral aneurysms. *International Journal for Numerical Methods in Fluids*, *58*(10), 1081–1100. doi:10.1002/fld.1786

Valencia, A., & Solis, F. (2006). Blood flow dynamics and arterial wall interaction in a saccular aneurysm model of the basilar artery. *Computers & Structures*, *84*(21), 1326–1337. doi:10.1016/j.compstruc.2006.03.008

Valencia, A., & Torres, F. (2017). Effects of hypertension and pressure gradient in a human cerebral aneurysm using fluid structure interaction simulations. *Journal of Mechanics in Medicine and Biology*, *17*(1), 1750018. doi:10.1142/S0219519417500180X

Varble, N., Xiang, J., Lin, N., Levy, E., & Meng, H. (2016). Flow instability detected by high-resolution computational fluid dynamics in fifty-six middle cerebral artery aneurysms. *Journal of Biomechanical Engineering*, *138*(6), 061009. doi:10.1115/1.4033477

Volokh, K. Y. (2008). Prediction of arterial failure based on a microstructural bi-layer fiber-matrix model with softening. *Journal of Biomechanics*, *41*(2), 447–453. doi:10.1016/j.jbiomech.2007.08.001

Voß, S., Glaßer, S., Hoffmann, T., Beuing, O., Weigand, S., Jachau, K., . . . Berg, P. (2016). Fluid-structure simulations of a ruptured intracranial aneurysm: Constant versus patient-specific wall thickness. *Computational and Mathematical Methods in Medicine*, *2016*, 9854539. doi:10.1155/2016/9854539

Zhang, Y., Chong, W., & Qian, Y. (2013). Investigation of intracranial aneurysm hemodynamics following flow diverter stent treatment. *Medical Engineering & Physics*, *35*(5), 608–615. doi:10.1016/j.mede